Materials and Design 155 (2018) 264–277

Contents lists available at ScienceDirect

Materials and Design

journal homepage: www.elsevier.com/locate/matdes

Generation and characterisation of gallium titanate surfaces through hydrothermal ion-exchange processes

Matthew D. Wadge *, Bryan W. Stuart, Kathryn G. Thomas, David M. Grant *

Advanced Materials Research Group, Faculty of Engineering, University of Nottingham, UK

HIGHLIGHTS

- Gallium (9.4 at.%) can successfully ion-exchange with sodium (2.7 at.%) in titanate structures (0.5–1 μm deep).
- RHEED analysis was successfully conducted, for the first time, confirming *d* spacing values for titanate structures.
- Pre-heat-treated gallium titanate (2.76 ppm) released more gallium ions compared to post-heat-treated samples (0.68 ppm).
- Released gallium ion concentrations (4–40 μM) were significantly less than toxic concentrations for *S. aureus* (0.3–5.1 mM).
- Gallium titanate showed significant (p<0.0001) cytotoxicity (76% cell viability reduction) vs. heat-treated layers (19% reduction).

GRAPHICAL ABSTRACT

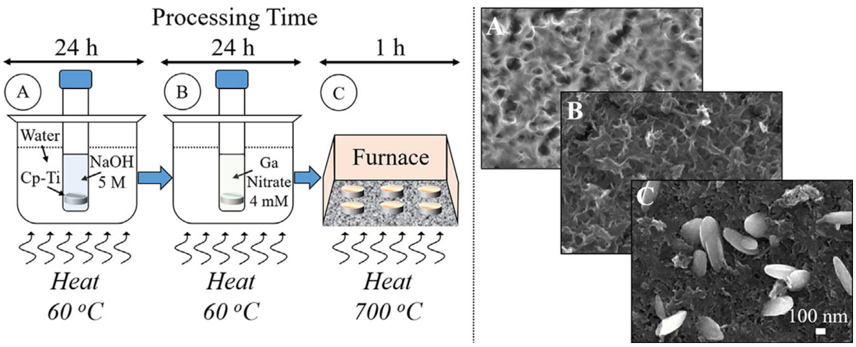

ARTICLE INFO

Article history:
Received 17 March 2018
Received in revised form 25 May 2018
Accepted 27 May 2018
Available online xxxx

Keywords:
Biomaterial
Sodium titanate
Gallium titanate
Hydrothermal
Ion-exchange
Titanium

ABSTRACT

Infection negation and biofilm prevention are necessary developments needed for implant materials. Furthermore, an increase in publications regarding gallium (Ga) as an antimicrobial ion has resulted in bacterial-inhibitory surfaces incorporating gallium as opposed to silver (Ag). The authors present the production of novel gallium titanate surfaces through hydrothermal ion-exchange reactions. Commercially-pure Ti (S0: Cp-Ti) was initially suspended in NaOH solutions to obtain sodium titanate (S1: Na_2TiO_3) layers *ca.* 0.5–1 μm in depth (2.4 at.% Na). Subsequent suspension in $Ga(NO_3)_3$ (S2: $Ga_2(TiO_3)_3$), and post-heat-treatment at 700 °C (S3: $Ga_2(TiO_3)_3$-HT), generated gallium titanate layers (9.4 and 4.1 at.% Ga, respectively). For the first time, RHEED analysis of gallium titanate layers was conducted and demonstrated titanate formation. Degradation studies in DMEM showed S2: $Ga_2(TiO_3)_3$ released more Ga compared to S3: $Ga_2(TiO_3)_3$-HT (2.76 *vs.* 0.68 ppm) over 168 h. Furthermore, deposition of Ca/P in a Ca:P ratio of 1.71 and 1.34, on S2: $Ga_2(TiO_3)_3$ and S3: $Ga_2(TiO_3)_3$-HT, respectively, over 168 h was seen. However, the study failed to replicate the antimicrobial effect presented by *Yamaguchi* who utilised *A. baumannii*, compared to *S. aureus* used presently. The authors feel a full antimicrobial study is required to assess gallium titanate as a candidate antimicrobial surface.

1. Introduction

The extent of a medical implant's success *in vivo* is dependent upon growth of extracellular tissue up to, and around, the implant *via*

---

* Corresponding authors.
E-mail addresses: matthew.wadge@nottingham.ac.uk (M.D. Wadge), david.grant@nottingham.ac.uk (D.M. Grant).

https://doi.org/10.1016/j.matdes.2018.05.060

osteoconduction and osteogenesis [1]. In recent years, significant emphasis has been directed towards improving adhesion between implant surfaces and local tissues through direct surface modifications [2–4].

The only FDA approved process for improving implant surfaces utilises high-temperature (droplet temperatures >1500 K [5]) plasma spray methods to deposit coatings of osteoconductive hydroxyapatite (HA) [6]; mimicking the main mineral component, and chemical and crystal structure, of cortical bone. These coatings, therefore, are ideal for improving metallic implant biocompatibility and enhancing osseointegration [7]. However, current plasma-spraying techniques offer poor adhesion [8]; non-uniformity in coating density [9]; excessive temperatures leading to deleterious phase transformations [10]; as well as residual surface stresses [11] resulting in micro-crack formation [12]. Ultimately, plasma-sprayed HA layers have been shown to spall due to their brittle nature [13], and weak mechanical adhesion (55–62 MPa; just higher than the FDA's minimum requirement of 50.8 MPa) [14,15]. Spalled particles may embed within surrounding tissue, activating complex cellular pathogenesis networks, fundamentally leading to periprosthetic osteolysis [16,17]; aseptic implant loosening [18]; and increased convalescence through necessitated revision surgery [19]. Further methods for providing a stable HA layer have been proposed, such as sputtering, but often have issues related to the crystal orientation, amorphous structure requiring subsequent treatments, or the relatively high manufacturing costs [20].

To overcome these limitations, solution-based surface treatments have been considered [21–23], including the production of sodium titanate surfaces [24]. Research by Kokubo et al. [25–32], identified the formation of sodium titanate through hydrothermal synthesis, therefore, preventing coating spallation caused by excessive production temperatures. Studies confirmed that optimal surface formation occurred at 60 °C, much lower than current plasma-spraying technologies. Once generated, and following further heat- and water-treatments, Ca and P ion-exchanges with the Na modifier within the sodium titanate structure occur. This allows HA generation upon implantation *in vivo* or submersion in simulated body fluid (SBF) *in vitro*, offering an attractive processing methodology [28].

Failure of implants still persists as a substantial issue in orthopaedic hip replacements, with most common factors including infection (25–28%), and mechanical loosening (19%) [33,34]. Implant infection is a complex issue as bacteria entering the surgical site adhere to implant surfaces and form a ‘biofilm’, protecting individual bacteria from antibiotics and the patient's immune system [35]. Initial prevention of biofilm formation is an attractive solution [36]. One possible method for biofilm prevention is the utilisation of antimicrobial ions, such as copper (Cu), silver (Ag), and more recently, gallium (Ga) [37,38].

Despite its prevalence, the use of Ag has been extensively debated in medical devices [39]. This is because there are conflicting results in the literature, for example various *in vitro* studies have demonstrated cytotoxic effects on host fibroblasts and keratinocytes [40,41], whilst others have shown minimal, to no, sequelae *in vivo* [42]. A review by Brett demonstrated the majority of *in vivo* studies indicate silver's non-cytotoxicity, however, its ability to bind to proteins and nucleic acids may result in higher topical dosages being needed to generate antimicrobial effects [39]. Furthermore, studies have shown Ag's limited capacity to fully protect against infections, which has resulted in increased concern for its use in medical devices [43].

Ga^{3+} ions have been purported to be an ideal substitute for Ag in antimicrobial surfaces through various anti-bacterial studies [44,45]. Their similarity to Fe^{3+} in ionic radius and charge, allow replacement within target molecules, which has resulted in an ideal antimicrobial agent, whose presence can cause Ga-induced bacterial metabolic distress [44,46]. A further property, which is pertinent to orthopaedic applications, is the inhibition of bone resorption through reduction in calcium release from bone [47]. Therefore, in this work, the authors present extensive characterisation of gallium titanate surfaces produced through ion-exchange reactions of sodium titanate produced *via* hydrothermal synthesis. In addition to cross-section electron microscopy, RHEED analysis on the top few nm of the titanate's surface, in conjunction with XPS of the same surface, to elucidate their structure and chemistry, is presented. Additionally, a pilot study to assess the cytotoxicity and antimicrobial nature of these surfaces is shown.

The antimicrobial nature of gallium titanate surfaces has been assessed previously by Yamaguchi et al. using a nosocomial, multidrug resistant, Gram-negative bacteria: *A. baumannii* [48], although using a different processing route. However, assessment using a Gram-positive bacteria of gallium titanate surfaces has yet to be investigated, hence the conducted pilot study using *S. aureus* (Newman). This is presented here along with the detailed characterisation and stability of using different hydrothermal conditions and concentrations compared to *Yamaguchi*, and its stability in media, pre- and post-heat-treatment, to fully understand the potential of this route.

Ion-exchange routes in low temperature solutions (60 °C) have the potential to enable low cost and scalable generation of osteogenic, antimicrobial surfaces, in comparison to plasma spraying and physical vapour deposition [28,30]. Another key advantage is its ability to manipulate surface chemistry reactions and utilise the ion-exchangeability of Na_2TiO_3 with ions including Ca, P, Mg, Ga, and Ag. This will enable further tailoring and design of surfaces, which could combine a customised array of therapeutic ions to treat individual requirements; a stratified approach to design [49–52]. Furthermore, solution based methodologies encourage sufficient penetration into porous morphologies to facilitate cellular infiltration, which is limited with conventional line of site coating methods [49].

2. Methodology

2.1. Substrate preparation

Commercially-pure Ti (Grade 1) discs (10 mm ∅, 1 mm thick), herein labelled as S0: Cp-Ti, were used as substrates. Discs were ground and polished using varying grits (P280, P400, P800, P1200, P2500 and P4000) of silicon carbide paper. The discs were cleaned by sonicating in acetone followed by distilled water for 5 min each.

2.2. Sodium hydroxide hydrothermal treatment

A 5 M solution of NaOH was prepared by dissolving 19.99 g of NaOH pellets (purity: 99.0%, Sigma-Aldrich) in 100 mL of distilled water. 10 mL aliquots in triplicate were then heated in water baths and individual S0: Cp-Ti substrates were placed in each polypropylene container at 60 °C for 24 h. Na-exchanged samples were labelled as S1: Na_2TiO_3.

2.3. Ion-exchange treatments

Gallium ion-exchange reactions were conducted from S1: Na_2TiO_3, using a 4 mM solution of $Ga(NO_3)_3$. The solution was prepared by dissolving 0.1 g of $Ga(NO_3)_3 \cdot xH_2O$ granules ($x = 1$–9) (purity: 99.9%, Sigma-Aldrich) into 100 mL of water. 10 mL aliquots in polypropylene containers were heated at 60 °C in water baths for 24 h. Ga-exchanged titanate samples have been labelled S2: $Ga_2(TiO_3)_3$.

2.4. Heat-treatments

Both S0: Cp-Ti and S2: $Ga_2(TiO_3)_3$ were heat-treated to produce S4: Cp-Ti-HT and S3: $Ga_2(TiO_3)_3$-HT, respectively, using a Lenton® furnace in air with a ramp rate of 5 $°C\ min^{-1}$ to 700 °C. All samples were left to dwell for 1 h followed by natural furnace cooling to room temperature.

2.5. Scanning electron microscopy (SEM)

Micrographs were obtained by Scanning Electron Microscopy (SEM) *via* a JEOL 6490LV SEM. A constant working distance of 10 mm was

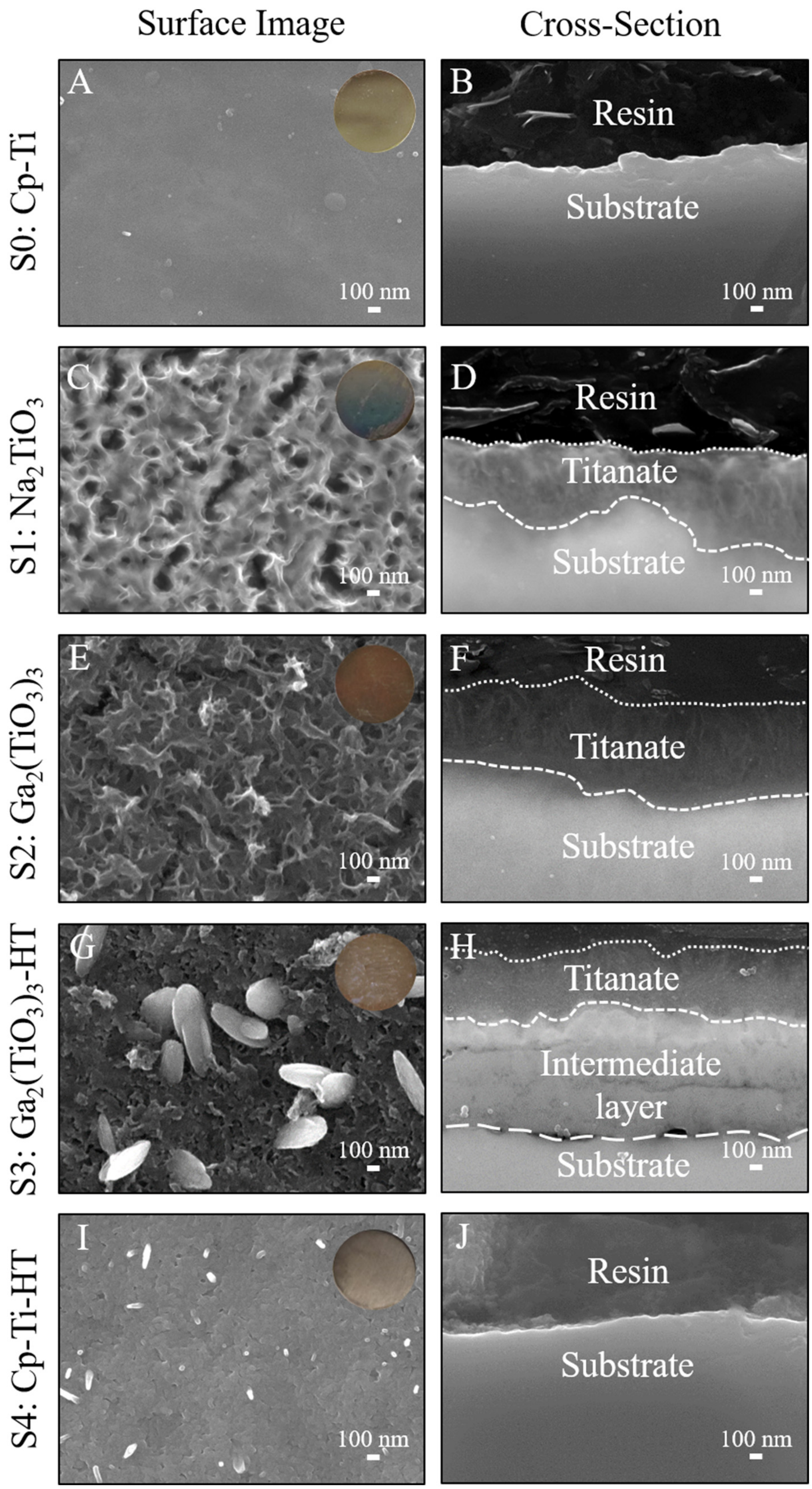

Fig. 1. (A, C, E, G, and I) FEG-SEM surface and (B, D, F, H, and J) cross-sectional images of S0: Cp-Ti, S1: Na_2TiO_3, S2: $Ga_2(TiO_3)_3$, S3: $Ga_2(TiO_3)_3$-HT, and S4: Cp-Ti-HT samples, respectively. Inset images are of the corresponding sample's surface.

maintained, utilising a beam energy of 15 kV. Image acquisitions for higher resolution scans were conducted on a Field-Emission Gun Scanning Electron Microscope (JEOL 7100 FEG-SEM).

2.6. Energy dispersive X-ray spectroscopy (EDX)

Surface compositional analysis was determined *via* an Energy-Dispersive X-ray spectrometer (EDX) (Oxford Instruments) at a working distance of 10 mm, a beam voltage of 15 kV, and maintaining a minimum X-ray count of 150,000 counts.

2.7. X-ray diffraction (XRD)

Crystallinity was assessed using a Bruker D8 advanced XRD spectrometer (Cu Kα source, $\lambda = 1.5406$ Å, 40 kV, 35 mA). Measurements were taken over a 2θ range from 25 to 65°; with a step size of 0.04° (2θ); a glancing angle of 2°; and a dwell time of 12 s. The glancing angle allows the X-ray beam to graze the surface, penetrating the first few microns of material, and restricting the diffraction signal to the same depth [53].

2.8. Reflective high-energy electron diffraction (RHEED)

Shallow angle diffraction analysis was conducted using a JEOL 2000 FX TEM with an attached RHEED stage and photographic plate camera. Film acquisition was obtained using an accelerating voltage of 200 kV, and an exposure time between 11 and 22 s to ensure visible diffraction rings were present. Diffraction ring radii were then analysed using an image processing software and appropriate *d* spacing values were calculated according to Bragg's law. Calibration was conducted using a sputtered gold layer on the surface of an S0: Cp-Ti substrate.

2.9. Raman spectroscopy

Raman spectroscopy was achieved utilising a HORIBA Jobin Yvon LabRAM HR spectrometer. Spectra were acquired using a 532 nm laser (25 mW power), 50× objective, and a 300 μm confocal pinhole. For simultaneous scanning of multiple Raman shifts, a 600 lines/mm rotatable diffraction grating along a path length of 800 mm was used. Detection of spectra was achieved through the use of a SYNAPSE CCD detector (1024 pixels) thermoelectrically cooled to −60 °C. Instrument calibration using the Rayleigh line at 0 cm^{-1} and a standard Si (100) reference band at 520.7 cm^{-1}, was employed prior to spectra acquisition. A constrained time window of 20 s was employed for each spectra recording with 20 accumulations.

2.10. Fourier transform infrared spectroscopy (FTIR)

Infrared absorbance was surveyed using a Bruker Tensor FTIR spectrometer with an Attenuated Total Reflectance (ATR) attachment containing a diamond crystal/ZnSe lens. λ of 2.5 to 20 μm were surveyed, corresponding to 4000 and 500 cm^{-1}, respectively.

2.11. X-ray photoelectron spectroscopy (XPS)

X-ray Photoelectron Spectroscopy (XPS) was conducted using a VG ESCALab Mark II X-ray photoelectron spectrometer with a monochromatic Al Kα X-ray source incident to the sample surface at ≈30°. Survey and high-resolution scans were conducted in addition to the measurement of adventitious C 1s for calibration: charge corrected to 284.8 eV. Parameters for acquisition were as follows: step size of 1.0; number of scans set at 5; dwell time 0.2 s for survey scans, and 0.4 s for high-resolution scans. Binding energies were measured over a range of 0–1200 eV. All spectra were analysed in Casa XPS constraining the Full Width at Half Maximum to the same value for all deconvoluted spectral peaks for the same element.

2.12. Ion leaching via induction coupled plasma (ICP)

Samples were degraded in 1 mL DMEM and were removed after varying degradation times of 6 h, 24 h, 3 days (72 h), and 7 days (168 h). During removal, the samples were washed with 9 mL of ultrapure water, ensuring a serum dilution of 1:10, before being removed and subsequently washed in ultrapure water and air dried. The 10 mL solutions were then analysed using inductively coupled plasma mass spectrometry (ICPMS; Thermo-Fisher Scientific iCAP-Q with CCTED). Each time point had three samples independently prepared, with calculated standard error and mean values presented.

2.13. Neutral red uptake (NRU) assay

Samples were degraded in 1 mL DMEM containing Fetal Bovine Serum for 7 days at 37 °C, generating liquid extracts as described in ISO 10993-5:2009. The extended degradation time was used to mimic long-term contact with the body. MG-63 cells were seeded into a 24 well plate (20,000 cells cm^{-2}) and incubated for 24 h to give a sub-confluent monolayer. The media was removed and replaced with the liquid extracts. After 24 h further incubation the media was removed, the cells washed with PBS, and 500 μL of Neutral Red medium was added. After 2 h incubation, the medium was removed, cells were washed in PBS, and 500 μL of de-stain was added per well. Plates were shaken on a plate shaker for 10 min and the NR absorption read using an ELx800 Microplate Colorimeter (BioTek Instruments Inc.) at 540 nm.

2.14. LIVE/DEAD assay

S2: $Ga_2(TiO_3)_3$ and S3: $Ga_2(TiO_3)_3$-HT samples alongside S0: Cp-Ti controls were sterilised *via* UVB light (Naure Class II Safety Cabinet) for 30 min per side. *S. aureus* Newman strain was cultured in Tryptone Soy Broth (TSB) overnight. Samples of each type were added in triplicate to sterile petri dishes and 15 mL pre-warmed (37 °C) TSB added. The overnight culture was washed twice in TSB, and then used to inoculate the petri dishes to 0.01 OD_{600}. The dishes were incubated (37 °C at 60 RPM) for 3 days, followed by washing in distilled water twice, then incubated at room temperature in the dark for 30 min with BacLight LIVE/DEAD stain (Invitrogen), and finally dried. The samples were imaged on a Carl Zeiss L700 Confocal Laser Scanning Microscope and biomass volume analysed *via* COMSTAT 2 plugin to ImageJ [54].

3. Results

3.1. Compositional analysis

3.1.1. SEM

Surface alterations were tracked following each ion-exchange reaction and post-heat-treatment. After NaOH treatment at 60 °C (S1: Na_2TiO_3), some alteration to the morphology of Ti surfaces from S0: Cp-Ti was exhibited (Fig. 1A & C). Extended nano-porous networks with features of the order of a few hundred nanometers in diameter were seen. Following Ga ion-exchange, micrographs of S2: $Ga_2(TiO_3)_3$

Table 1
EDX elemental mapping data of S0: Cp-Ti, S1: Na_2TiO_3, S2: $Ga_2(TiO_3)_3$, S3: $Ga_2(TiO_3)_3$-HT, and S4: Cp-Ti-HT samples over a 400 μm^2 area of the sample surface. Mean atomic percent (at.%) are shown with standard error (S.E.M.; $n = 3$).

Sample	Elemental composition / at.%			
	Ti	O	Na	Ga
S0: Cp-Ti	100	0	0	0
S1: Na_2TiO_3	31.9 ± 0.1	65.3 ± 0.1	2.7 ± 0.2	0
S2: $Ga_2(TiO_3)_3$	20.1 ± 0.2	70.5 ± 0.3	0	9.4 ± 0.1
S3: $Ga_2(TiO_3)_3$-HT	22.6 ± 0.4	73.3 ± 0.4	0	4.1 ± 0.2
S4: Cp-Ti-HT	30.2 ± 0.1	69.8 ± 0.1	0	0

showed a similar interconnected morphology to S1: Na_2TiO_3 (Fig. 1E). Upon heat-treatment (S3: $Ga_2(TiO_3)_3$-HT), a slightly modified interconnected morphology remained, with the formation of flake-like features on the surface, with diameters of 150–300 nm (Fig. 1G). The inclusion of S4: Cp-Ti-HT (Fig. 1I), was to identify morphological differences between sodium titanate and rutile formation on the sample's surface. The surface of S3: $Ga_2(TiO_3)_3$-HT was significantly dissimilar to that of S4: Cp-Ti-HT with a porous angular surface containing oblong flakes of *ca.* 0.5 μm.

Cross-sectional FEG-SEM imaging of S1: Na_2TiO_3, S2: $Ga_2(TiO_3)_3$, and S3: $Ga_2(TiO_3)_3$-HT showed similar morphology, with a distinct porous layer of the order of 0.5–1 μm in thickness (Fig. 1D. F, & H). This is in stark contrast to the original smooth S0: Cp-Ti control sample (Fig. 1B). However, the layer exhibited in S3: $Ga_2(TiO_3)_3$-HT demonstrates an intermediate layer between the nanoporous surface layer and the titanium substrate (Fig. 1H). Furthermore, S4: Cp-Ti-HT demonstrated a different cross-sectional profile to all other samples with a thin, dense titanium oxide layer (Fig. 1J).

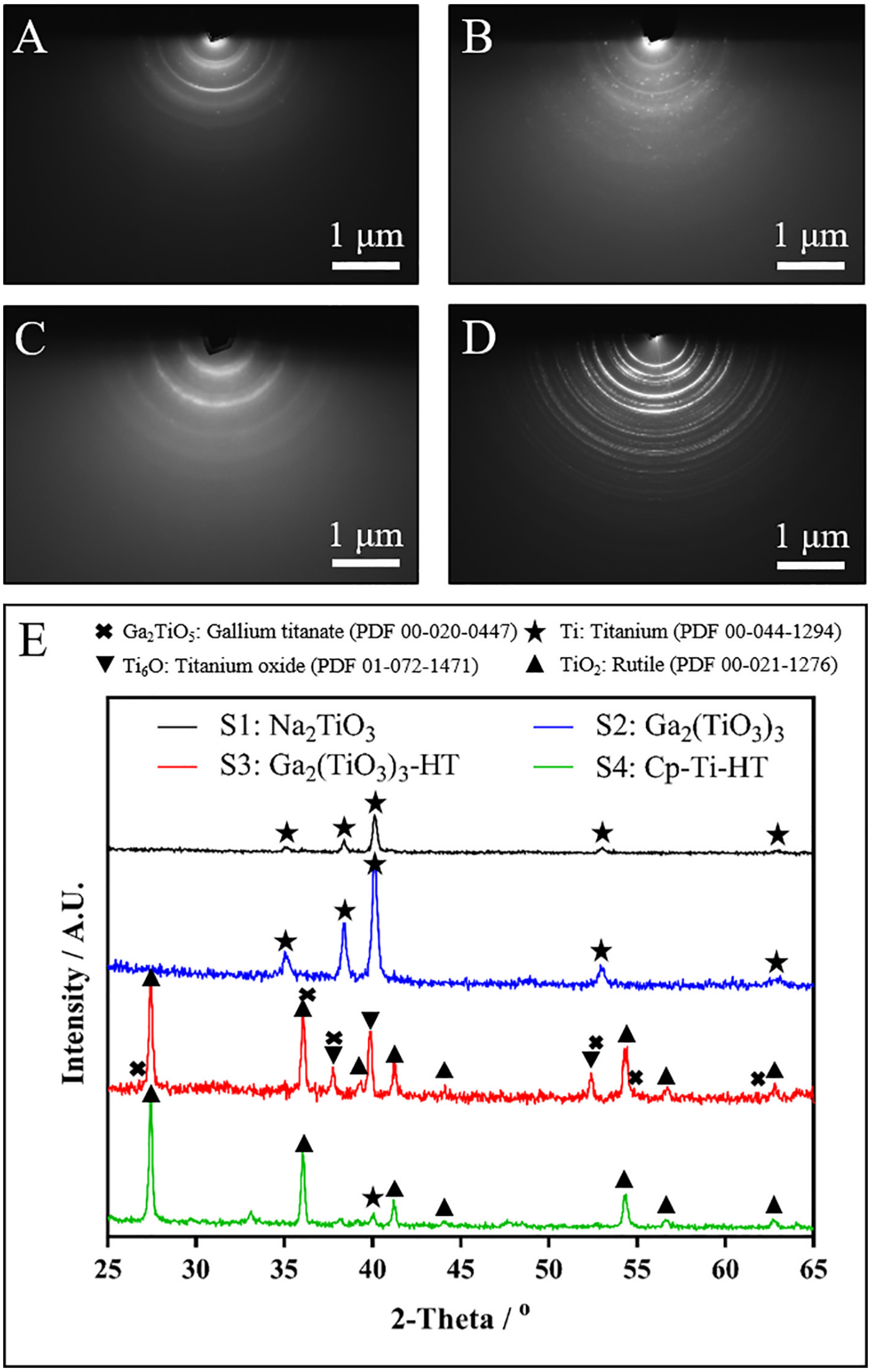

Fig. 2. (A, B, C and D) RHEED diffraction patterns for S1: Na_2TiO_3, S2: $Ga_2(TiO_3)_3$, S3: $Ga_2(TiO_3)_3$-HT, and S4: Cp-Ti-HT, respectively. (E) XRD data of aforementioned samples. Deconvolution of the peaks are as follows: ▲ - rutile (TiO_2: ICDD PDF 00-021-1276); ▼ - titanium oxide (Ti_6O: ICDD PDF 01-072-1471); ✖ – gallium titanate (Ga_2TiO_5: ICDD PDF 00-020-0447); ★ - titanium (Ti: ICDD PDF 00-044-1294).

Table 2
Quantitative RHEED analysis data for calculated *d* spacing (using principles from Bragg's law) figures compared to database values. Calculated *d* spacing values all have standard errors <0.01. Ring radii and *d* spacing data has been rounded to 3 s.f.

Sample	Database file	Calculated *d* spacing / Å	Database *d* spacing / Å
S1: Na_2TiO_3	Sodium titanate ($Na_{0.23}TiO_2$) (ICDD PDF 00-022-1404)	3.70	3.65
		1.87	1.92
	Titanium (Ti) (ICDD PDF 00-044-1294)	2.28	2.24
	Sodium titanate (Na_4TiO_4) (ICDD PDF 00-042-0513)	3.22	3.23
		2.28	2.21
		1.87	1.87
S2: $Ga_2(TiO_3)_3$	Calcium titanate ($CaTi_2O_5$) (ICDD PDF 00-025-1450)	3.50	3.50
		1.83	1.87
	Sodium titanate (Na_2TiO_3) (ICDD PDF 00-037-0346)	3.27	3.23
		1.83	1.87
S3: $Ga_2(TiO_3)_3$-HT	Gallium titanate (Ga_2TiO_5) (ICDD PDF 01-070-1993)	3.50	3.38
		2.88	2.75
	Calcium titanate ($CaTi_2O_5$) (ICDD PDF 00-025-1450)	3.50	3.50
		2.88	2.92
		1.82	1.87
S4: Cp-Ti-HT	Rutile (TiO_2) (ICDD PDF 00-021-1276)	3.23	3.25
		2.45	2.49
		2.28	2.30
		2.19	2.19
		2.05	2.05

3.1.2. EDX

Initially, elemental mapping analysis of S1: Na_2TiO_3 showed homogeneous distribution of Na, Ti and O, and concluded Na (2.73 at.%) and O (65.3 at.%) had been included within the structure, compared to the S0: Cp-Ti control. Subsequent analysis of S2: $Ga_2(TiO_3)_3$ indicated complete substitution of Na by Ga within the TiO_3 structure. S2: $Ga_2(TiO_3)_3$ compared to S3: $Ga_2(TiO_3)_3$-HT showed a 5.3 at.% reduction of Ga within the later following heat-treatment (Table 1).

3.1.3. XRD

As seen in Fig. 2E, the only signals present for S1: Na_2TiO_3 and S2: $Ga_2(TiO_3)_3$ were that of the Ti substrate (S0: Cp-Ti), which produced peaks associated with titanium (Ti: ICDD PDF 00-044-1294). Following heat-treatment (S3: $Ga_2(TiO_3)_3$-HT), further diffraction peaks emerged located at ≈26, 36, 38, and 55° 2θ, which were attributed to gallium titanate (Ga_2TiO_5: ICDD PDF 00-020-0447), however, the lack of high quality diffraction data for gallium titanate, the lower intensity, as well as the overlap of gallium titanate with rutile means XRD data alone is inconclusive. The peak at ≈57° 2θ correlated to rutile (TiO_2: ICDD PDF 00-021-1276), and peaks at ≈37, 40, and 53° 2θ related to titanium oxide (Ti_6O: ICDD PDF 01-072-1471). To verify this further, RHEED analysis was conducted as this technique offers greater probing resolution and shallower probing depth (0.1–10 nm) as compared to XRD (0.1–100 μm) [53,55].

3.1.4. RHEED

RHEED analysis of S4: Cp-Ti-HT (Fig. 2D) demonstrated clear and distinct diffraction rings, as well as matching *d* spacing values with rutile (TiO_2: ICDD PDF 00-021-1276: Table 2) consistent with the SEM-EDX and XRD results. The diffraction patterns present in S1: Na_2TiO_3, S2: $Ga_2(TiO_3)_3$, and S3: $Ga_2(TiO_3)_3$-HT (Fig. 2A, B, and C, respectively) demonstrated a significant change from that of S4: Cp-Ti-HT, indicating an alternative layer to rutile (Fig. 2D). The *d* spacing values for S1: Na_2TiO_3 were ascribed to sodium titanate ($Na_{0.23}TiO_2$: ICDD PDF 00-022-1404, and Na_4TiO_4: ICDD PDF 00-042-0513) and titanium (Ti: ICDD PDF 00-044-1294). Furthermore, S2: $Ga_2(TiO_3)_3$ *d* spacing values were akin to calcium and sodium titanate variants ($CaTi_2O_5$: ICDD PDF 00-025-1450, and Na_2TiO_3: ICDD PDF 00-037-0346), as well as S3: $Ga_2(TiO_3)_3$-HT being similar to gallium and calcium titanate variants (Ga_2TiO_5: ICDD PDF 01-070-1993, and $CaTi_2O_5$: ICDD PDF 00-025-1450).

3.1.5. Raman

Raman spectral analysis (Fig. 3A) of S3: $Ga_2(TiO_3)_3$-HT and S4: Cp-Ti-HT revealed bands located at ≈247, 445, and 611 cm^{-1}, which were attributed to rutile, Ti—O. Conversely, alternate peaks were found in the S2: $Ga_2(TiO_3)_3$ sample at ≈273, 425, 700, and 811 cm^{-1}, as well as ≈400 and 662 cm^{-1} in S1: Na_2TiO_3. A shoulder was present in both S3: $Ga_2(TiO_3)_3$-HT and S4: Cp-Ti-HT at ≈700 cm^{-1}, which was also present as an identifiable peak in S2: $Ga_2(TiO_3)_3$.

3.1.6. FTIR

IR absorption showed peaks detailed from 500 to 900 cm^{-1}, matching TiO_6 vibrations, Ti—O bending and Ti—OH non-bridging bonds, which were prevalent across all samples (Fig. 3B). Additionally, a peak around 1100 cm^{-1} and a broad peak from 3000 to 3500 cm^{-1}, which appear in S1: Na_2TiO_3 and S2: $Ga_2(TiO_3)_3$, correspond to Ti—O—C vibrations and H—O—H stretching, respectively. Three peaks at 1130, 1300, and 2350 cm^{-1} were seen in the S4: Cp-Ti-HT control, consistent with rutile Ti—O, Ti—O—Ti stretching, and CO_2 contamination, respectively. The peak at 2050 cm^{-1} remains unmatched. Doublet peaks around 2880 cm^{-1} in S3: $Ga_2(TiO_3)_3$-HT, matched C—H furnace contamination. Finally, all spectra except S4: Cp-Ti-HT exhibited a peak around 1610–1630 cm^{-1}, consistent with O—H bonds.

3.1.7. XPS

XPS analysis of S1: Na_2TiO_3, S2: $Ga_2(TiO_3)_3$, and S3: $Ga_2(TiO_3)_3$-HT samples was conducted (Fig. 4). The initial O 1s peak (Fig. 4A) at

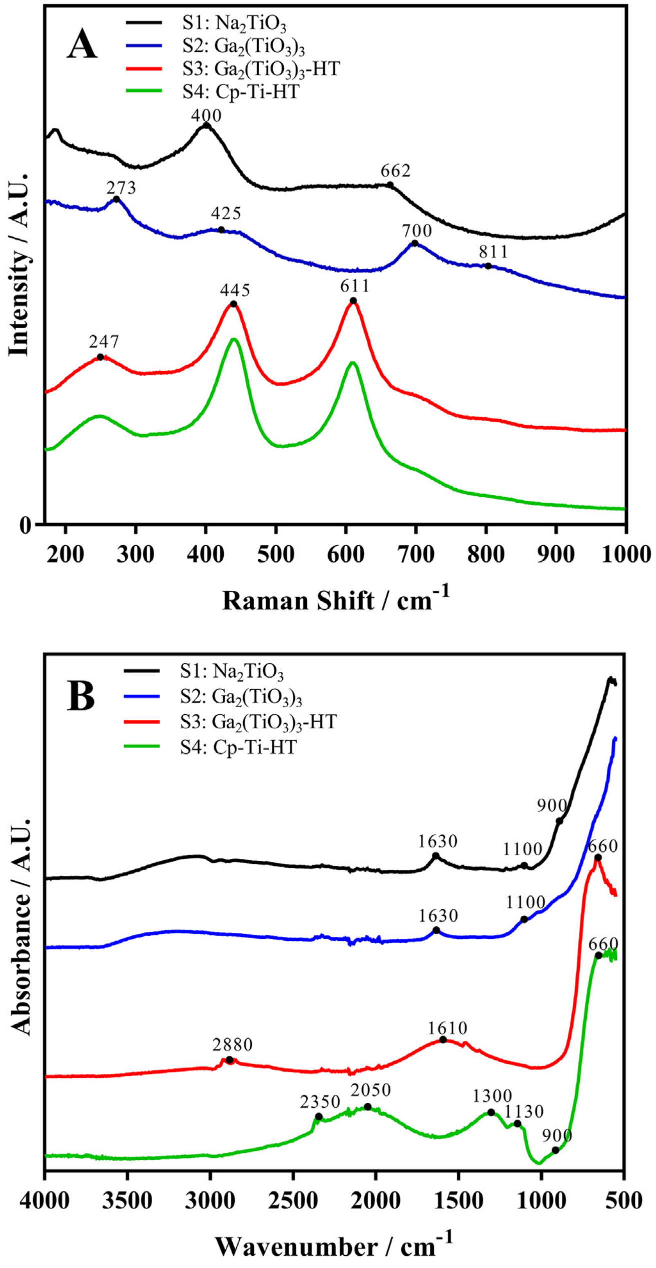

Fig. 3. (A) Raman infrared spectroscopy analysis, and (B) FTIR analysis of S1: Na_2TiO_3, S2: $Ga_2(TiO_3)_3$, S3: $Ga_2(TiO_3)_3$-HT, and S4: Cp-Ti-HT samples.

529.6 eV in the S1: Na_2TiO_3 sample exhibited a shift to 531.6 eV and 530.7 eV in S2: $Ga_2(TiO_3)_3$ and S3: $Ga_2(TiO_3)_3$-HT, respectively. Deconvolution of O 1s for S1: Na_2TiO_3 demonstrated three peaks at 530.2, 531.6, and 532.9 eV, with area ratios of 75.0, 15.3, and 9.7%, respectively. Each peak matched O—Ti^{4+}, O—Ti^{3+}, and —OH, respectively. This reduced to two peaks at 530.3 (49.3%) and 531.9 (50.7%) eV in the S2: $Ga_2(TiO_3)_3$ sample, eliminating —OH. Moreover, S3: $Ga_2(TiO_3)_3$-HT demonstrated two peaks, with shifts to 530.7 (82.4%) and 532.4 (17.6%) eV, eliminating O—Ti^{3+}.

A perceptible shift was noted in the Ti 2p doublet peak (Fig. 4B) for S3: $Ga_2(TiO_3)_3$-HT. Initial positions at 458.6 and 464.3 eV, corresponded to Ti 2p 3/2 and Ti 2p 1/2 in the S1: Na_2TiO_3 sample. These shifted to 458.5 and 464.2 eV in S2: $Ga_2(TiO_3)_3$. However, a further shift to 459.0 and 464.7 eV was observed in S3: $Ga_2(TiO_3)_3$-HT, which all correspond to Ti^{4+}. The Na 1s peak at 1071.9 eV (Fig. 4C), matching Na—O, in the S1: Na_2TiO_3 sample (Ti LMM Auger peaks located at 1067.3 and 1075.1 eV), diminished after Ga ion-exchange in both S2: $Ga_2(TiO_3)_3$ and S3: $Ga_2(TiO_3)_3$-HT. Furthermore, the Ga 2p doublet peak (Fig. 4D) showed distinct peaks at 1118.3 and 1145.2 eV, corresponding to Ga 2p 3/2 and Ga 2p 1/2 for Ga^{4+}—O, respectively, in S2: $Ga_2(TiO_3)_3$; and 1118.4 and 1145.3 eV, respectively, in S3: $Ga_2(TiO_3)_3$-HT.

3.1.8. Degradation and ion leaching

Fig. 5(A–F) demonstrated the surface alteration of S2: $Ga_2(TiO_3)_3$ and S3: $Ga_2(TiO_3)_3$-HT samples after degradation in 1 mL DMEM over 168 h. It is clear, compared to surfaces illustrated in Fig. 1, that surface deposition/growth occurred during degradation, as well as opening of the porous surface network. Spherical deposits were seen on both S2: $Ga_2(TiO_3)_3$ and S3: $Ga_2(TiO_3)_3$-HT at 24 and 72 h. EDX analysis of the deposits demonstrated their composition to be rich in Ca and P. Ca:P ratios were then taken, as demonstrated in Fig. 5G, with S3: $Ga_2(TiO_3)_3$-HT resulting in a surface Ca:P ratio close to 1.34, whereas S2: $Ga_2(TiO_3)_3$ reached 1.71 by 168 h. Furthermore, rod-like deposits were also seen on both samples at 24 and 72 h. Their composition, as delineated by EDX, consisted mainly of Ga and O, suggesting Ga_2O_3 had deposited. By 168 h, the surface morphology (Fig. 5E & F) showed an absence of both spherical and rod-like surface growths in S2: $Ga_2(TiO_3)_3$, and larger clusters of rod-like deposits had formed on S3: $Ga_2(TiO_3)_3$-HT.

A combination of EDX and ICP (Fig. 6) was used to identify the alteration of both surface and solution ion concentrations during DMEM degradation. Over 168 h, aqueous Ga ion concentrations gradually increased for S3: $Ga_2(TiO_3)_3$-HT (Fig. 6D) as expected, however, at a slower rate than S2: $Ga_2(TiO_3)_3$ (Fig. 6B), with a peak Ga ion concentration of 2.76 and 0.68 ppm for S2: $Ga_2(TiO_3)_3$ and S3: $Ga_2(TiO_3)_3$-HT, respectively. The error at 168 h in S2: $Ga_2(TiO_3)_3$ meant quantification here was difficult. Additionally, S2: $Ga_2(TiO_3)_3$ surface Ga concentration (Fig. 6A) decreased over the course of 168 h, whereas the S3: $Ga_2(TiO_3)_3$-HT sample (Fig. 6C) demonstrated a re-deposition of Ga during the later time points. For both S2: $Ga_2(TiO_3)_3$ and S3: $Ga_2(TiO_3)_3$-HT, Ca and P aqueous ion concentrations decreased between 0 and 168 h (Fig. 6B & D). Both surface Ca and P ion concentrations increased for S2: $Ga_2(TiO_3)_3$, however, S2: $Ga_2(TiO_3)_3$ (Fig. 6A) exhibited deposition and subsequent re-release during the 168 h period (Fig. 6C).

3.1.9. Cell studies

From ISO 10993-5:2009, the definition of a cytotoxic effect demonstrated by an NRU assay is a >30% reduction in cell viability from the non-treated cells (Tissue Culture Plastic (TCP) control). The dotted line in Fig. 7 shows this threshold at 70% signal intensity. The untreated S0: Cp-Ti sample demonstrated an average signal of 94.2%, with S2: $Ga_2(TiO_3)_3$ and S3: $Ga_2(TiO_3)_3$-HT showing average signals of 24.2% and 81.4%, respectively. Therefore, both S0: Cp-Ti and S3: $Ga_2(TiO_3)_3$-HT samples are above the viability threshold, with a clear reduction in cell viability noted for the S2: $Ga_2(TiO_3)_3$ sample. It was shown through a One-way ANOVA, followed by the Bonferroni post-test that the S2: $Ga_2(TiO_3)_3$ sample, was the only sample that exhibited a significant difference ($p < 0.0001$) from the TCP control.

3.1.10. Live/dead

Biofilm development assay results are shown in Fig. 8, with no significant difference being noted between the live or dead biomass on any of the samples. The presence of dead bacteria on the Ti control sample is expected due to the length of the incubation period. An antimicrobial effect would be shown either by a significantly reduced total signal (both live and dead) from either titanate structures compared to the S0: Cp-Ti control, or by a significant decrease in live (green) signal and subsequent increase in dead (red) signal. Neither of these effects was prevalent in the data shown and was also not observed when the experiment was repeated.

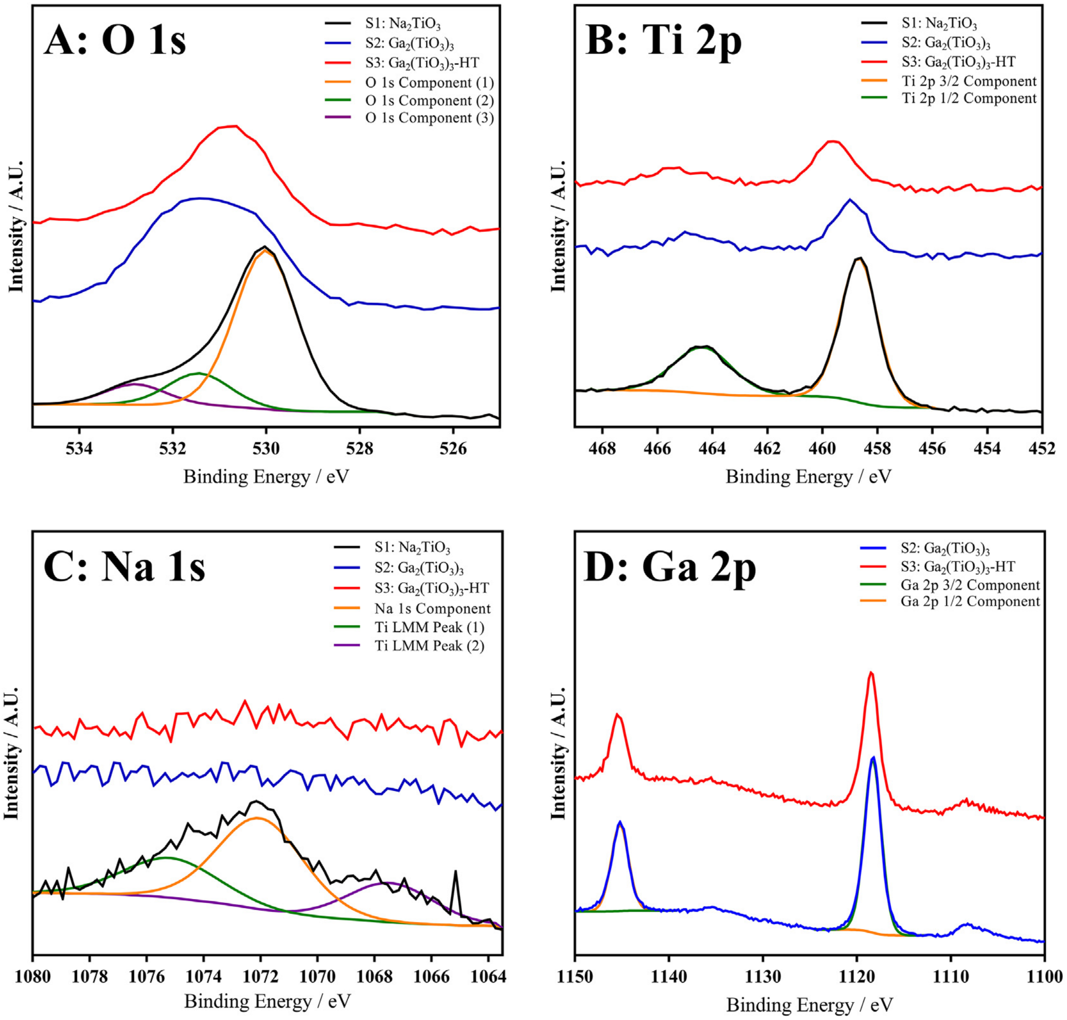

Fig. 4. XPS analysis of S1: Na$_2$TiO$_3$, S2: Ga$_2$(TiO$_3$)$_3$, and S3: Ga$_2$(TiO$_3$)$_3$-HT. (A) High-resolution O 1s spectra, (B) High-resolution Ti 2p spectra, (C) High-resolution Na 1s spectra, and (D) High-resolution Ga 2p spectra.

4. Discussion

4.1. Composition and topographical analysis by SEM, FEG-SEM, EDX, FTIR, XRD, XPS, and Raman

Ion-exchange reactions were a key development in the production of tailored, application specific titanate surfaces. This is due to the initial, layered sodium hydrogen titanate, formed from the NaOH treatment, allowing ion incorporation and substitution with Na$^+$ ions already present. Not only are these surfaces able to release ions into the surrounding media, but they can also facilitate further ion-exchange reactions *in vivo*, allowing generation of amorphous calcium phosphate layers, or release of therapeutic or antimicrobial ions.

The nanoporous surface morphology exhibited by S1: Na$_2$TiO$_3$ and S2: Ga$_2$(TiO$_3$)$_3$ was consistent with the only other gallium titanate study published [48] and the higher resolution presented here clearly shows interesting differences from the S0: Cp-Ti control, where no significant features were present. Initially, the sodium hydrogen titanate and the isomorphic gallium hydrogen titanate formed after ion-exchange, exhibited an open, nanoporous morphology. Upon heat-treatment, the surface layers increased in thickness, as well as becoming denser, upon conversion to gallium titanate. Furthermore, flake-like features (∅ ≈ 100–150 nm), formed of Ga and O from EDX analysis (Fig. 1G & Table 1), suggested gallium oxide/hydroxide formation. However, morphologically these features are significantly different to the gallium oxide precipitates noted on the degraded surfaces (Fig. 5). A study by Dulda et al. demonstrated micrographs of GaO(OH) precipitates formed through alkali precipitation, which morphologically are similar to the flake-like precipitates on S3: Ga$_2$(TiO$_3$)$_3$-HT [56] and correlates with the GaO(OH) peak noted in FTIR (Fig. 3B), suggesting these are GaO(OH) flakes. EDX analysis demonstrated no sodium was detectable on either gallium-treated samples, matching the lack of a Na 1s peak in XPS, indicating gallium ions readily ion-exchange with sodium in the titanate structure, supporting the postulated ion-exchangeability. The atomic percent of Ga exhibited in S2: Ga$_2$(TiO$_3$)$_3$ was 9.4 at.%; much greater than sodium (2.7 at.%) in S1: Na$_2$TiO$_3$. The surface features formed on S3: Ga$_2$(TiO$_3$)$_3$-HT are significantly different to S4: Cp-Ti-HT (Fig. 1), showing clear structural differences between the nanoporous titanate layers and the dense, smooth rutile formed during heat-treatment.

The XRD results suggested the initial hydrothermally produced (S1: Na$_2$TiO$_3$), and ion-exchanged layers (S2: Ga$_2$(TiO$_3$)$_3$) were amorphous in nature, since no additional crystalline peaks, further to the S0: Cp-Ti control, were present, correlating with the diffuse ring patterns noted in RHEED (Fig. 2). This was to be expected as no heat-treatment had been conducted, therefore, the surface layer produced should be amorphous; crystallisation temperature >500 °C [57]. Smaller, less intense, peaks were noted in XRD, with the lower intensities potentially attributed to lower quantities of surface crystals, due to the temperature being below the stated crystallisation temperature of gallium titanate (≈1100 °C [58]). However, this evidence alone was not conclusive, due to significant overlap with rutile, to identify the formation of

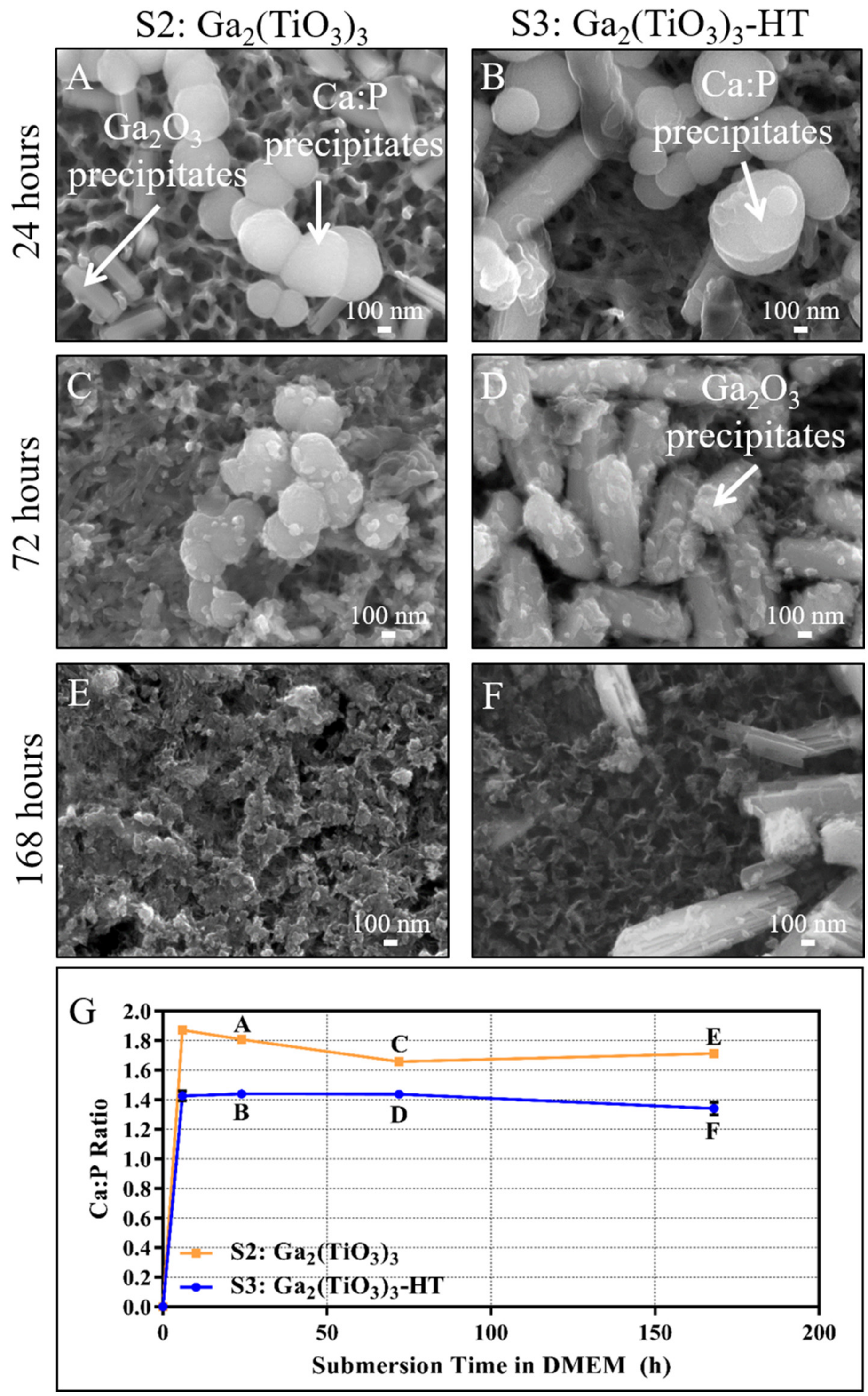

Fig. 5. (A, C, and E) FEG-SEM images of the surface of degraded S2: $Ga_2(TiO_3)_3$ samples in 1 mL DMEM (diluted with 1:10 ratio of ultrapure water) at time points 24, 72, and 168 h, respectively. (B, D, and F) FEG-SEM images of the surface of degraded S3: $Ga_2(TiO_3)_3$-HT samples at 24, 72, and 168 h, respectively. (G) Graph showing the alteration in Ca:P ratio on the surface of S2: $Ga_2(TiO_3)_3$ and S3: $Ga_2(TiO_3)_3$-HT during the degradation study. Ca:P rich nodules and Ga_2O_3 precipitates were observed.

titanate layers, and hence RHEED analysis was also conducted. This enabled shallower beam penetration, of the order of a few tens of nanometers, as well as higher probing resolution (0.01–0.001 nm) [55].

Upon heat-treatment (S3: $Ga_2(TiO_3)_3$-HT), the sample yielded new Bragg peaks corresponding to rutile: a characteristic phase transformation of titanium at >600 °C in oxygen, as anticipated [59]. Formation of rutile was also seen in the S4: Cp-Ti-HT sample, in the RHEED *d* spacing analysis, as well as two characteristic peaks detailed in FTIR (Fig. 3B), and three in Raman spectroscopy (Fig. 3A). Furthermore, smaller Bragg peaks at 26, 36, 38 and 55° 2θ from the XRD patterns, were deconvoluted as gallium titanate derivatives, partially confirming its formation. To avoid characterising just the rutile produced in S3: $Ga_2(TiO_3)_3$, as well as the Ti substrate in S1: Na_2TiO_3 and S2: $Ga_2(TiO_3)_3$, and allow characterisation of solely the produced surface layers, RHEED was employed. RHEED has a similar probing depth to the XPS used and, therefore, provides an ideal technique to compare and

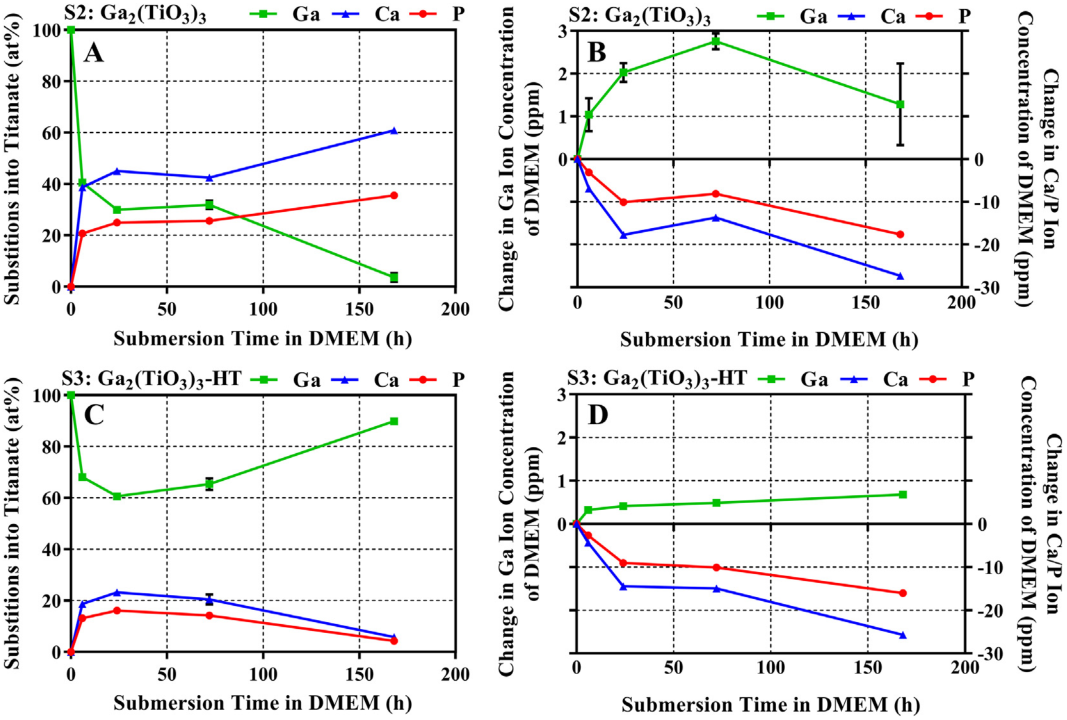

Fig. 6. (A & C) EDX analysis of the substitution of Ca, P, and Ga ions on the surface of S2: $Ga_2(TiO_3)_3$ and S3: $Ga_2(TiO_3)_3$-HT during 168 h of degradation, respectively. (B & D) ICP analysis of Ca, P, and Ga ion alterations of S2: $Ga_2(TiO_3)_3$ and S3: $Ga_2(TiO_3)_3$-HT in DMEM solution during degradation over 168 h, respectively. Error bars of S.E.M. ($n = 3$), with EDX taken over a 3600 μm^2 area.

corroborate results. As seen in Fig. 2D, RHEED demonstrates a clear diffraction pattern for rutile on S4: Cp-Ti-HT, and matches *d* spacing values from the database, as well as confirming the results from XPS (Fig. 4). Rutile diffraction rings were not observed in S3: $Ga_2(TiO_3)_3$-HT. However, even with RHEED, it was noted that the S1: Na_2TiO_3, S2: $Ga_2(TiO_3)_3$, and S3: $Ga_2(TiO_3)_3$-HT samples exhibited a more diffuse pattern than S4: Cp-Ti-HT only, causing overlap and complicated the quantification. This diffuseness could be attributed to the amorphous sodium or gallium hydrogen titanate layers present. Despite the diffuse rings, quantification of *d* spacing values was possible for S1: Na_2TiO_3, S2: $Ga_2(TiO_3)_3$, and S3: $Ga_2(TiO_3)_3$-HT, which matched sodium titanate derivatives ($Na_{0.23}TiO_2$ and Na_4TiO_4) and titanium; calcium and sodium titanate variants ($CaTi_2O_5$ and Na_2TiO_3); and gallium and calcium titanate derivatives (Ga_2TiO_5 and $CaTi_2O_5$) also suggested by [48], respectively.

The evidence demonstrated through XRD and RHEED was supported by IR absorption spectroscopy (Fig. 3B), which demonstrated characteristic TiO_6 octahedron vibrations, Ti—O bond stretching and Ti—OH non-bridging bonds of titanate structures. Edge-sharing TiO_6 octahedra and Ti—O—Ti stretching were also present in the Raman analysis [60–62]. Additionally, XPS also supported titanate formation, through the presence of Ti^{4+}—O bonding [63], which were ubiquitous across all samples, in both the Ti 2p and O 1s deconvolution, and are characteristic of titanate structures, as discussed by Takadama et al. [64].

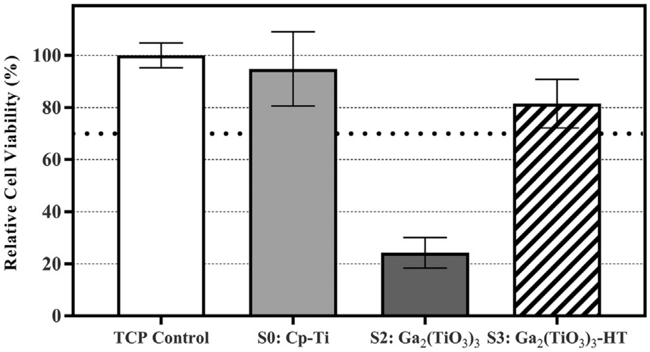

Fig. 7. Effect of elution products of S0: Cp-Ti, S2: $Ga_2(TiO_3)_3$ and S3: $Ga_2(TiO_3)_3$-HT samples, compared to the TCP control, on the viability of MG-63 cells measured by an NRU assay. All values are mean values ± S.E.M. ($n = 6$). Dotted line represents 70% threshold for cytotoxic effects (ISO 10993-5:2009).

Specifically for S1: Na_2TiO_3, there were no other FTIR absorption bonds corresponding to sodium titanate formation, however, this may be attributed to limitations on the FTIR spectrometer used, which made analysis lower than 600 cm^{-1} difficult [65]. Nevertheless, FTIR ruled out formation of re-precipitated NaOH, due to the lack of characteristic O—H tension peaks around 3600 cm^{-1} [66]. Despite this, Raman (Fig. 3A) and XPS analysis confirmed the presence of Na—O bonds, which are readily seen in sodium titanate structures [67]. The additional presence of O—H bending modes in Raman (as described by Oleksak et al. [68]), and —OH bonds in XPS, before and after heat-treatment, suggest amorphous sodium and gallium hydrogen titanate may also be present on the surface.

The shoulder exhibited between 800 and 900 cm^{-1}, shown in FTIR for S2: $Ga_2(TiO_3)_3$, may have corresponded to GaO(OH) vibrations and Ga—OH bending modes, which could be attributed to gallium hydrogen titanate formation prior to heat-treatment, as well as the GaO(OH) flakes noted in Fig. 1G [56,69]. Furthermore, peaks demonstrated by Raman spectroscopy may correspond to gallium oxide, as shown by Zhao et al. [70], Rao et al. [71], and Gao et al. [72], or derivatives of gallium titanate. The Raman peak at 700 cm^{-1} remains as a shoulder in S3: $Ga_2(TiO_3)_3$-HT, and correlates with the GaO(OH) flakes seen in Fig. 1G. Gallium titanate formation is also confirmed by XPS analysis, with the Ga 2p 3/2 peak position at ≈1118.5 eV relating to Ga—O in its Ga^{4+} state, which are doped at various characteristic Ti^{4+} sites, as detailed by Deng et al. [73]. Furthermore, the presence of Ti—O Raman bonds in S2: $Ga_2(TiO_3)_3$, suggest gallium titanate formation [74]. A significant alteration, which correlates well with the EDX results previously mentioned, is the reduction in the Na 1s peak in XPS for both S2: Ga_2

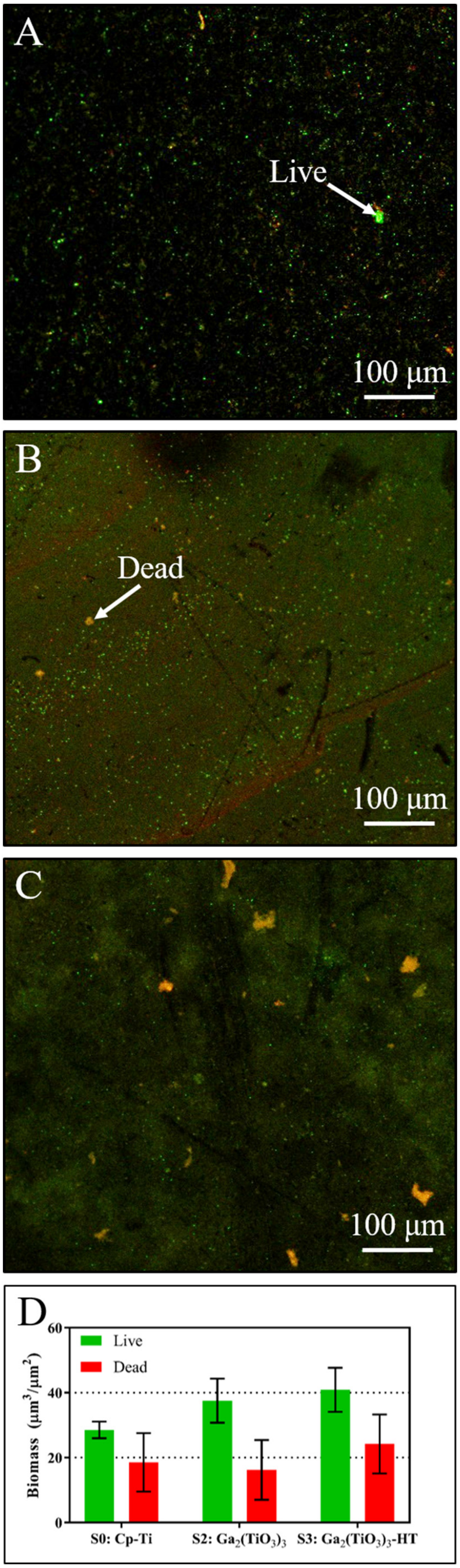

Fig. 8. (A, B, and C) LIVE/DEAD staining maps for S0: Cp-Ti, S2: $Ga_2(TiO_3)_3$, and S3: $Ga_2(TiO_3)_3$-HT, respectively. Live bacteria are stained green, with dead bacteria stained red, as indicated. (D) Live and dead biomass from a 3 day culture of *S. aureus* analysed *via* COMSTAT. There is no significant difference between the live or dead values between the samples (2 way ANOVA). The experiment was repeated and the same trends observed ($n = 3$; error bars in S.E.M.).

$(TiO_3)_3$ and S3: $Ga_2(TiO_3)_3$-HT, demonstrating complete Na replacement, and the subsequent formation of gallium titanate.

In addition to titanate formation, broad absorption peaks from 3000 to 3500 cm^{-1}, seen in both S1: Na_2TiO_3 and S2: $Ga_2(TiO_3)_3$, can be ascribed to H—O—H stretch bonds of any remaining surface, or chemisorbed/interlamellar water, since this stage was prior to the heat-treatment step [75]. The removal of these peaks in both heat-treated samples: S3: $Ga_2(TiO_3)_3$-HT and S4: Cp-Ti-HT, support this postulation and is further backed up by Shiropur et al., who showed peak elimination during dehydration [60]. Interestingly, FTIR demonstrated a peak at 1100 cm^{-1} in both S1: Na_2TiO_3 and S2: $Ga_2(TiO_3)_3$, potentially matching Ti—O—C vibrations, which is unexpected, as the carbon location would be in place of either gallium or sodium in the titanate structure [76]. It is evident from the heat-treatment stage, through the generation of doublet peaks at 2880 cm^{-1} (S3: $Ga_2(TiO_3)_3$-HT) and the shoulder at 2350 cm^{-1} in FTIR, matching C—H bonds and atmospheric CO_2, respectively, that carbon contamination on the surface of the samples is present and unavoidable [77].

4.2. Surface degradation and ion release

During submersion in DMEM, opening of the porous network in the titanate surfaces was observed. Furthermore, spherical and rod-like deposits, which through EDX analysis were found to be formed of Ca:P and Ga:O, respectively, were also noted (Fig. 5). Morphologically, the rod-like Ga:O deposits look similar to those generated by Zhao et al. and Shah et al. [78,79]. Deposition may have occurred due to over-saturation of the surrounding solution, however, further studies would be needed to confirm this postulation. Additional EDX analysis was conducted on the Ca and P deposits to understand the Ca:P ratio, and whether these deposits were similar to HA. For S2: $Ga_2(TiO_3)_3$, the Ca:P ratio increased significantly above 1.8 within 6 h and gradually plateaued at 1.71 by 7 days. This is in stark contrast to the heat-treated sample (S3: $Ga_2(TiO_3)_3$-HT), which had a Ca:P ratio of ≈1.42 at 6 h and reached a final ratio of 1.34 by 7 days. Stoichiometric HA contains a Ca:P = 1.67, with calcium deficient and calcium rich HA having ratios of <1.67 and >1.67, respectively [80]. Correlating this with the Ca:P generated on both samples, S2: $Ga_2(TiO_3)_3$ and S3: $Ga_2(TiO_3)_3$-HT are calcium rich and calcium deficient, respectively. Studies conducted by Kizuki et al. demonstrated the relative propensity for ion inclusion into the titanate layer for Ca^{2+} and Na^+ [81]. The studies concluded that, even with a calcium contamination of 0.0005% in the sodium containing solution, divalent Ca^{2+} ions would preferentially enter into the structure, as it has a more potent electrostatic attraction to negative TiO_6 [82]. The authors hypothesise that the calcium contained within the solution, preferentially ion-exchanged into the surface layer due to its relatively higher propensity, as demonstrated through literature studies investigating Ca^{2+} ions preferentially exchanging into the titanate structure [27,28,83]. As S2: $Ga_2(TiO_3)_3$ has a less stable layer compared to S3: $Ga_2(TiO_3)_3$-HT, due to the increased release rate of Ga ions, this explains why there is a higher Ca content on S2: $Ga_2(TiO_3)_3$.

The opening of the porous network, as well as the deposition of Ca:P and Ga_2O_3 exhibited in the micrograph images (Fig. 5) correlates with the ICP and EDX analysed ionic alterations on the sample's surface and in solution. As shown in Fig. 6, S3: $Ga_2(TiO_3)_3$-HT released gallium at a much slower rate than S2: $Ga_2(TiO_3)_3$, suggesting the heat-treatment had a significant effect on the stability of the titanate surface generated. Moreover, the peak Ga solution concentration was much greater for S2:

$Ga_2(TiO_3)_3$ (2.76 ppm; day 3) compared to S3: $Ga_2(TiO_3)_3$-HT (0.68 ppm; day 7). Additionally, the trend in surface concentration of Ga in Fig. 6 agrees well with the micrographs presented in Fig. 5. The S2: $Ga_2(TiO_3)_3$ sample exhibited an overall decrease in Ga ions with no deposition occurring, whereas S3: $Ga_2(TiO_3)_3$-HT demonstrated a deposition of Ga back onto the surface after 24 h, with a large proportion of Ga:O deposits. Furthermore, the decrease in solution ionic concentrations of Ca and P, as well as the overall increase of these ions on S2: $Ga_2(TiO_3)_3$, relates to the deposition of Ca:P deposits seen in Fig. 5. The anomalous re-release of Ca and P from the surface of S3: $Ga_2(TiO_3)_3$-HT, which does not match the solution concentration, could be due to detachment of Ca:P precipitates, which are not detectable *via* ICP. Distinction between Ca ions penetrating into the titanate layer and deposition on the surface was not possible with the techniques used, hence further studies would be needed.

The mechanism for amorphous calcium phosphate formation, and subsequent apatite maturation, has been explained previously [27,84]. The surface titanate layers, containing positive metallic ions, with this case being Ga^{3+}, facilitate ionic exchange between H_3O^+ (hydronium) ions and Ga^{3+}. This exchange generates Ti—OH bonds upon the top surface of the titanate layers, generating an overall negative surface charge. This negative charge allows Ca^{2+} ions to preferentially ion-exchange into the surface. High concentration of Ca^{2+} ions on the surface generates an overall positive surface charge, allowing phosphate ions present within the DMEM solution to be attracted to the surface, generating calcium phosphate precipitates (Fig. 5). Since S3: $Ga_2(TiO_3)_3$-HT contained a heat-treatment stage and, therefore, had a more stable surface layer, Ga release was much lower than S2: $Ga_2(TiO_3)_3$ (Fig. 6), which evidently resulted in lower consumption of Ca ions from the DMEM onto the surface (Figs. 5 & 6). This is evident in the calcium-deficient Ca:P precipitates present on S3: $Ga_2(TiO_3)_3$-HT, as well as the smaller quantity of precipitates present on the surface (Fig. 5).

Although the relationship between heat-treatment temperatures and Ga release was not investigated here, the conversion of a sodium titanate hydrogel following heat-treatments was the subject of a previous study by Kim et al. Their findings showed that the progressive increase in heat-treatment temperatures converted the gel into an amorphous and crystalline sodium titanate at 400 and 700 °C, respectively, reducing its reactivity and propensity to form apatite in simulated body fluid [83]. It is postulated that Ga ion release would decline with increases in heat-treatment temperatures in a similar manner.

4.3. Cytotoxicity and antimicrobial assessment

Initial evaluation on the effect of titanate surfaces on human (MG-63) cells has been performed *via* a Neutral Red Uptake assay. Upon exposure to media, which had been in contact with the samples for 7 days, significant reduction in cell viability was only shown for S2: $Ga_2(TiO_3)_3$, with the performance of S0: Cp-Ti, S3: $Ga_2(TiO_3)_3$-HT and cells exposed to untreated media showing no significant differences (Fig. 7). From the ICP analysis, the maximum Ga release for the S2: $Ga_2(TiO_3)_3$ and S3: $Ga_2(TiO_3)_3$-HT samples were 2.76 and 0.68 ppm (39.6 and 18.6 μM), respectively. Although these concentrations are lower than those commonly seen in the literature for Ga toxicity to human cells, the hypothesis that the heat-treatment stabilising the rate of gallium release is supported by these results [85,86]. The toxicity of Ga can also be effected by local Fe concentrations and any binding molecules, which can promote Ga uptake into the cells. It is also possible that a toxic pH was caused by the elutant of the S2: $Ga_2(TiO_3)_3$ samples during ion-exchange within the structure; an effect which is lost after heat-treatment.

In this pilot study, *S. aureus* was used as it is a clinically relevant pathogen commonly associated with nosocomial, and orthopaedic biofilm, infections, occurring in as many as 75% of joint infections [87–89]. Although Ga has been demonstrated to be antimicrobial against a wide variety of pathogens, its efficacy varies over a wide range of inhibitory concentrations (μM–mM) specific to each bacterial strain. An antimicrobial effect of gallium titanate structures against *A. baumannii* has been recently demonstrated by Yamaguchi et al. [48]. *A. baumannii* has been found to be particularly susceptible to Ga (2–100 μM), whereas *S. aureus* is relatively more resistant compared to other species (0.32–5.12 mM) [44,90]. Although the concentration of gallium used to produce these structures was far higher than in the *Yamaguchi* study, these results suggest that it has still fallen short of the minimum inhibitory concentration to prevent a *S. aureus* infection. In DMEM, the Ga release after 6 h was 1.04 and 0.32 ppm for S2: $Ga_2(TiO_3)_3$ and S3: $Ga_2(TiO_3)_3$-HT, respectively (15 and 4.6 μM in 1 mL solution), which falls well below the toxic concentrations for *S. aureus*, in addition to being considerably lower than concentrations clinically used [91]. However, upon reflection, the authors feel it is necessary to conduct a further, more comprehensive, study to fully elucidate the antimicrobial status of gallium titanate surfaces against *S. aureus* and other common nosocomial pathogens.

5. Conclusions

Formation of gallium titanate surfaces through sequential hydrothermal NaOH, $Ga(NO_3)_3$ and subsequent heat-treatments, was successful. Full characterisation of the produced gallium titanate surfaces was conducted, using FEG-SEM, RHEED, XRD, XPS, FTIR, EDX, Raman, and ICP methodologies. Significant morphological changes were demonstrated at high-resolution on titanium surfaces upon hydrothermal treatment in NaOH, ion-exchange in $Ga(NO_3)_3$, and subsequent heat-treatment. Furthermore, the antimicrobial and cytotoxic nature of the produced surfaces were assessed *via* Neutral red and LIVE/DEAD analyses. In addition to the Ga ion's ability to substitute into the sodium titanate structure, the surface layer enables release of Ga ions into the surrounding environment. However, further testing against a wider range of relevant pathogens is required in order to demonstrate the concentrations of Ga necessary for these surfaces to be clinically effective. It is also clear that the heat-treatment conducted on the gallium titanate surface resulted in a more stable layer that released Ga ions at a slower rate: 2.76 compared to 0.68 ppm for S2: $Ga_2(TiO_3)_3$ and S3: $Ga_2(TiO_3)_3$-HT, respectively. Further to this, the incorporation of Ca/P ions on the surface was much lower on the heat-treated surface (S3: $Ga_2(TiO_3)_3$-HT), generating a calcium deficient amorphous precipitate (Ca:P = 1.34), relative to crystalline HA, and as compared to the calcium rich (Ca:P = 1.71) precipitate deposited on the surface of S2: $Ga_2(TiO_3)_3$.

If additional assessments can indicate microbiological and further osteogenic efficacy, such surfaces may be suitable candidates as an orthopaedic alternative. The production design, which utilised low temperature Ga ion-exchange reactions, will enable tailorable and cost effective antimicrobial surfaces that can potentially be used to coat both surfaces and internal porosities of orthopaedic prosthetics at commercial scales; a key design improvement.

Acknowledgements

This work was supported by the Engineering and Physical Sciences Research Council [grant numbers EP/K029592/1, EP/L022494/1]; and the EPSRC Centre for Innovative Manufacturing in Medical Devices (MeDe Innovation). The authors would like to gratefully acknowledge the Nanoscale and Microscale Research Centre (nmRC) at the University of Nottingham for SEM, FEG-SEM and Raman access, as well as Dr. N. C. Neate for his help in RHEED acquisition and analysis, and Dr. G. A. Rance for Raman technical assistance. We would also like to gratefully acknowledge Saul Vazquez Reina for assistance with ICP-MS analysis.

Conflict of interests

The authors declare that there is no conflict of interest regarding the publication of this paper.

Data availability

The raw/processed data required to reproduce these findings cannot be shared at this time as the data also forms part of an ongoing study.

References

[1] M. Geetha, A. Singh, R. Asokamani, A. Gogia, Ti based biomaterials, the ultimate choice for orthopaedic implants–a review, Prog. Mater. Sci. 54 (3) (2009) 397–425.

[2] R. Tejero, E. Anitua, G. Orive, Toward the biomimetic implant surface: biopolymers on titanium-based implants for bone regeneration, Prog. Polym. Sci. 39 (7) (2014) 1406–1447.

[3] G. Thakral, R. Thakral, N. Sharma, J. Seth, P. Vashisht, Nanosurface–the future of implants, J. Clin. Diagn. Res. 8 (5) (2014) ZE07.

[4] V. Goriainov, R. Cook, J.M. Latham, D.G. Dunlop, R.O. Oreffo, Bone and metal: an orthopaedic perspective on osseointegration of metals, Acta Biomater. 10 (10) (2014) 4043–4057.

[5] Y. Tsui, C. Doyle, T. Clyne, Plasma sprayed hydroxyapatite coatings on titanium substrates part 1: mechanical properties and residual stress levels, Biomaterials 19 (22) (1998) 2015–2029.

[6] R.A. Surmenev, M.A. Surmeneva, A.A. Ivanova, Significance of calcium phosphate coatings for the enhancement of new bone osteogenesis–a review, Acta Biomater. 10 (2) (2014) 557–579.

[7] R. Agarwal, A.J. García, Biomaterial strategies for engineering implants for enhanced osseointegration and bone repair, Adv. Drug Deliv. Rev. 94 (2015) 53–62.

[8] E. Mohseni, E. Zalnezhad, A.R. Bushroa, Comparative investigation on the adhesion of hydroxyapatite coating on Ti–6Al–4V implant: a review paper, Int. J. Adhes. Adhes. 48 (2014) 238–257.

[9] J.L. Ong, D.L. Carnes, K. Bessho, Evaluation of titanium plasma-sprayed and plasma-sprayed hydroxyapatite implants in vivo, Biomaterials 25 (19) (2004) 4601–4606.

[10] L. Sun, C.C. Berndt, C.P. Grey, Phase, structural and microstructural investigations of plasma sprayed hydroxyapatite coatings, Mater. Sci. Eng. A 360 (1) (2003) 70–84.

[11] S. Takeuchi, M. Ito, K. Takeda, Modelling of residual stress in plasma-sprayed coatings: effect of substrate temperature, Surf. Coat. Technol. 43 (1990) 426–435.

[12] X. Zheng, M. Huang, C. Ding, Bond strength of plasma-sprayed hydroxyapatite/Ti composite coatings, Biomaterials 21 (8) (2000) 841–849.

[13] V. Rattan, T. Sidhu, M. Mittal, Study and characterization of mechanical and electrochemical corrosion properties of plasma sprayed hydroxyapatite coatings on AISI 304L stainless steel, J. Biomimetics, Biomater. Biomed. Eng. (2018) 20–34 Trans Tech Publ.

[14] K. De Groot, R. Geesink, C. Klein, P. Serekian, Plasma sprayed coatings of hydroxylapatite, J. Biomed. Mater. Res. A 21 (12) (1987) 1375–1381.

[15] T.J. Callahan, J. Gantenberg, B.E. Sands, Calcium phosphate (Ca-P) coating draft guidance for preparation of Food and Drug Administration (FDA) submissions for orthopedic and dental endosseous implants, Characterization and Performance of Calcium Phosphate Coatings for Implants, ASTM International, 1994.

[16] E. Sukur, Y.E. Akman, Y. Ozturkmen, F. Kucukdurmaz, Particle disease: a current review of the biological mechanisms in periprosthetic osteolysis after hip arthroplasty, Open Orthop. J. 10 (2016) 241.

[17] J.A. Broomfield, T.T. Malak, G.E. Thomas, A.J. Palmer, A. Taylor, S. Glyn-Jones, The relationship between polyethylene wear and periprosthetic osteolysis in total hip arthroplasty at 12 years in a randomized controlled trial cohort, J. Arthroplast. 32 (4) (2017) 1186–1191.

[18] L. Sun, C.C. Berndt, K.A. Gross, A. Kucuk, Material fundamentals and clinical performance of plasma-sprayed hydroxyapatite coatings: a review, J. Biomed. Mater. Res. A 58 (5) (2001) 570–592.

[19] N.P. Hailer, S. Lazarinis, K.T. Mäkelä, A. Eskelinen, A.M. Fenstad, G. Hallan, L. Havelin, S. Overgaard, A.B. Pedersen, F. Mehnert, Hydroxyapatite coating does not improve uncemented stem survival after total hip arthroplasty! An analysis of 116,069 THAs in the Nordic Arthroplasty Register Association (NARA) database, Acta Orthop. 86 (1) (2015) 18–25.

[20] J. Jansen, J. Wolke, S. Swann, J. Van Der Waerden, K. De Groof, Application of magnetron sputtering for producing ceramic coatings on implant materials, Clin. Oral Implants Res. 4 (1) (1993) 28–34.

[21] L. Le Guéhennec, A. Soueidan, P. Layrolle, Y. Amouriq, Surface treatments of titanium dental implants for rapid osseointegration, Dent. Mater. 23 (7) (2007) 844–854.

[22] D. Melilli, N. Mauceri, Surface treatments for titanium implants, Int. J. Clin. Dent. 8 (2) (2015).

[23] S. Bahl, A.S. Krishnamurthy, S. Suwas, K. Chatterjee, Controlled nanoscale precipitation to enhance the mechanical and biological performances of a metastable β Ti-Nb-Sn alloy for orthopedic applications, Mater. Des. 126 (2017) 226–237.

[24] S. Nishiguchi, S. Fujibayashi, H.M. Kim, T. Kokubo, T. Nakamura, Biology of alkali-and heat-treated titanium implants, J. Biomed. Mater. Res. A 67 (1) (2003) 26–35.

[25] T. Kokubo, Apatite formation on surfaces of ceramics, metals and polymers in body environment, Acta Mater. 46 (7) (1998) 2519–2527.

[26] T. Kokubo, Design of bioactive bone substitutes based on biomineralization process, Mater. Sci. Eng. C 25 (2) (2005) 97–104.

[27] T. Kokubo, H.-M. Kim, M. Kawashita, Novel bioactive materials with different mechanical properties, Biomaterials 24 (13) (2003) 2161–2175.

[28] T. Kokubo, H.-M. Kim, M. Kawashita, T. Nakamura, Review bioactive metals: preparation and properties, J. Mater. Sci. Mater. Med. 15 (2) (2004) 99–107.

[29] T. Kokubo, T. Matsushita, H. Takadama, Titania-based bioactive materials, J. Eur. Ceram. Soc. 27 (2) (2007) 1553–1558.

[30] T. Kokubo, S. Yamaguchi, Bioactive titanate layers formed on titanium and its alloys by simple chemical and heat treatments, Open Biomed. Eng. J. 9 (1) (2015).

[31] T. Kokubo, S. Yamaguchi, Growth of novel ceramic layers on metals via chemical and heat treatments for inducing various biological functions, Front. Bioeng. Biotechnol. 3 (2015).

[32] H. Takadama, H.M. Kim, T. Kokubo, T. Nakamura, TEM-EDX study of mechanism of bonelike apatite formation on bioactive titanium metal in simulated body fluid, J. Biomed. Mater. Res. A 57 (3) (2001) 441–448.

[33] K.J. Bozic, A.F. Kamath, K. Ong, E. Lau, S. Kurtz, V. Chan, T.P. Vail, H. Rubash, D.J. Berry, Comparative epidemiology of revision arthroplasty: failed THA poses greater clinical and economic burdens than failed TKA, Clin. Orthop. Relat. Res. 473 (6) (2015) 2131–2138.

[34] M. Sundfeldt, L.V. Carlsson, C.B. Johansson, P. Thomsen, C. Gretzer, Aseptic loosening, not only a question of wear: a review of different theories, Acta Orthop. 77 (2) (2006) 177–197.

[35] J. Costerton, L. Montanaro, C. Arciola, Biofilm in implant infections: its production and regulation, Int. J. Artif. Organs 28 (11) (2005) 1062–1068.

[36] J. Hasan, S. Jain, R. Padmarajan, S. Purighalla, V.K. Sambandamurthy, K. Chatterjee, Multi-scale surface topography to minimize adherence and viability of nosocomial drug-resistant bacteria, Mater. Des. 140 (2018) 332–344.

[37] J.L. Hobman, L.C. Crossman, Bacterial antimicrobial metal ion resistance, J. Med. Microbiol. 64 (5) (2015) 471–497.

[38] Y. Su, S. Champagne, A. Trenggono, R. Tolouei, D. Mantovani, H. Hermawan, Development and characterization of silver containing calcium phosphate coatings on pure iron foam intended for bone scaffold applications, Mater. Des. 148 (2018) 124–134.

[39] D.W. Brett, A discussion of silver as an antimicrobial agent: alleviating the confusion, Ostomy Wound Manage 52 (1) (2006) 34–41.

[40] B.S. Atiyeh, M. Costagliola, S.N. Hayek, S.A. Dibo, Effect of silver on burn wound infection control and healing: review of the literature, Burns 33 (2) (2007) 139–148.

[41] M.M. Cortese-Krott, M. Münchow, E. Pirev, F. Heβner, A. Bozkurt, P. Uciechowski, N. Pallua, K.-D. Kröncke, C.V. Suschek, Silver ions induce oxidative stress and intracellular zinc release in human skin fibroblasts, Free Radic. Biol. Med. 47 (11) (2009) 1570–1577.

[42] C. Coombs, A. Wan, J. Masterton, R. Conyers, J. Pedersen, Y. Chia, Do burn patients have a silver lining? Burns 18 (3) (1992) 179–184.

[43] A. Politano, K. Campbell, L. Rosenberger, R. Sawyer, Use of silver in the prevention and treatment of infections: silver review, Surg. Infect. 14 (1) (2013) 8–20.

[44] F. Minandri, C. Bonchi, E. Frangipani, F. Imperi, P. Visca, Promises and failures of gallium as an antibacterial agent, Future Microbiol 9 (3) (2014) 379–397.

[45] A. Cochis, B. Azzimonti, C. Della Valle, E. De Giglio, N. Bloise, L. Visai, S. Cometa, L. Rimondini, R. Chiesa, The effect of silver or gallium doped titanium against the multidrug resistant *Acinetobacter baumannii*, Biomaterials 80 (2016) 80–95.

[46] Y. Kaneko, M. Thoendel, O. Olakanmi, B.E. Britigan, P.K. Singh, The transition metal gallium disrupts *Pseudomonas aeruginosa* iron metabolism and has antimicrobial and antibiofilm activity, J. Clin. Invest. 117 (4) (2007) 877.

[47] T.J. Hall, T.J. Chambers, Gallium inhibits bone resorption by a direct effect on osteoclasts, Bone Miner. 8 (3) (1990) 211–216.

[48] S. Yamaguchi, S. Nath, Y. Sugawara, K. Divakarla, T. Das, J. Manos, W. Chrzanowski, T. Matsushita, T. Kokubo, Two-in-one biointerfaces—antimicrobial and bioactive nanoporous gallium titanate layers for titanium implants, Nanomaterials 7 (8) (2017) 229.

[49] X.-B. Chen, Y.-C. Li, J. Du Plessis, P.D. Hodgson, C.e. Wen, Influence of calcium ion deposition on apatite-inducing ability of porous titanium for biomedical applications, Acta Biomater. 5 (5) (2009) 1808–1820.

[50] S. Yamaguchi, T. Matsushita, T. Kokubo, A bioactive Ti metal with a Ca-enriched surface layer releases Mg ions, RSC Adv. 3 (28) (2013) 11274–11282.

[51] S. Yamaguchi, T. Kizuki, H. Takadama, T. Matsushita, T. Nakamura, T. Kokubo, Formation of a bioactive calcium titanate layer on gum metal by chemical treatment, J. Mater. Sci. Mater. Med. 23 (4) (2012) 873–883.

[52] T. Kizuki, T. Matsushita, T. Kokubo, Antibacterial and bioactive calcium titanate layers formed on Ti metal and its alloys, J. Mater. Sci. Mater. Med. 25 (7) (2014) 1737–1746.

[53] C. Giannini, M. Ladisa, D. Altamura, D. Siliqi, T. Sibillano, L. De Caro, X-ray diffraction: a powerful technique for the multiple-length-scale structural analysis of nanomaterials, Crystals 6 (8) (2016) 87.

[54] A. Heydorn, A.T. Nielsen, M. Hentzer, C. Sternberg, M. Givskov, B.K. Ersbøll, S. Molin, Quantification of biofilm structures by the novel computer program COMSTAT, Microbiology 146 (10) (2000) 2395–2407.

[55] S. Hasegawa, Reflection high-energy electron diffraction, Characterization of Materials, 2012.

[56] A. Dulda, Morphology controlled synthesis of α-GaO (OH) nanoparticles: thermal conversion to Ga_2O_3 and photocatalytic properties, Adv. Mater. Sci. Eng. 2016 (2016).

[57] C.Y. Kim, T. Sekino, K. Niihara, Synthesis of bismuth sodium titanate nanosized powders by solution/sol–gel process, J. Am. Ceram. Soc. 86 (9) (2003) 1464–1467.

[58] M. Mohammadi, D. Fray, Semiconductor TiO_2–Ga_2O_3 thin film gas sensors derived from particulate sol–gel route, Acta Mater. 55 (13) (2007) 4455–4466.

[59] K. Thamaphat, P. Limsuwan, B. Ngotawornchai, Phase characterization of TiO2 powder by XRD and TEM, Kasetsart J. (Nat. Sci.) 42 (5) (2008) 357–361.

[60] M. Shirpour, J. Cabana, M. Doeff, New materials based on a layered sodium titanate for dual electrochemical Na and Li intercalation systems, Energy Environ. Sci. 6 (8) (2013) 2538–2547.

[61] T.M. Marques, O.P. Ferreira, J.A. da Costa, K. Fujisawa, M. Terrones, B.C. Viana, Study of the growth of CeO2 nanoparticles onto titanate nanotubes, J. Phys. Chem. Solids 87 (2015) 213–220.

[62] R. Ma, K. Fukuda, T. Sasaki, M. Osada, Y. Bando, Structural features of titanate nanotubes/nanobelts revealed by Raman, X-ray absorption fine structure and electron diffraction characterizations, J. Phys. Chem. B 109 (13) (2005) 6210–6214.

[63] J. Chen, G. Zou, H. Hou, Y. Zhang, Z. Huang, X. Ji, Pinecone-like hierarchical anatase TiO2 bonded with carbon enabling ultrahigh cycling rates for sodium storage, J. Mater. Chem. A 4 (32) (2016) 12591–12601.

[64] H. Takadama, H.-M. Kim, T. Kokubo, T. Nakamura, XPS study of the process of apatite formation on bioactive Ti–6Al–4V alloy in simulated body fluid, Sci. Technol. Adv. Mater. 2 (2) (2001) 389–396.

[65] B.C. Viana, O.P. Ferreira, A.G. Souza Filho, J. Mendes Filho, O.L. Alves, Structural, morphological and vibrational properties of titanate nanotubes and nanoribbons, J. Braz. Chem. Soc. 20 (1) (2009) 167–175.

[66] M. Lillo-Ródenas, D. Cazorla-Amorós, A. Linares-Solano, Understanding chemical reactions between carbons and NaOH and KOH: an insight into the chemical activation mechanism, Carbon 41 (2) (2003) 267–275.

[67] L.L. Marciniuk, P. Hammer, H.O. Pastore, U. Schuchardt, D. Cardoso, Sodium titanate as basic catalyst in transesterification reactions, Fuel 118 (2014) 48–54.

[68] R.P. Oleksak, W.F. Stickle, G.S. Herman, Aqueous-based synthesis of gallium tungsten oxide thin film dielectrics, J. Mater. Chem. C 3 (13) (2015) 3114–3120.

[69] M.M. Can, G.H. Jaffari, S. Aksoy, S.I. Shah, T. Fırat, Synthesis and characterization of ZnGa$_2$O$_4$ particles prepared by solid state reaction, J. Alloys Compd. 549 (2013) 303–307.

[70] Y. Zhao, R.L. Frost, Raman spectroscopy and characterisation of α-gallium oxyhydroxide and β-gallium oxide nanorods, J. Raman Spectrosc. 39 (10) (2008) 1494–1501.

[71] R. Rao, A. Rao, B. Xu, J. Dong, S. Sharma, M. Sunkara, Blueshifted Raman scattering and its correlation with the [110] growth direction in gallium oxide nanowires, J. Appl. Phys. 98 (9) (2005), 094312.

[72] Y. Gao, Y. Bando, T. Sato, Y. Zhang, X. Gao, Synthesis, Raman scattering and defects of β-Ga$_2$O$_3$ nanorods, Appl. Phys. Lett. 81 (12) (2002) 2267–2269.

[73] Q. Deng, Y. Gao, X. Xia, R. Chen, L. Wan, G. Shao, V and Ga Co-Doping Effect on Optical Absorption Properties of TiO2 Thin Films, Journal of Physics: Conference Series, IOP Publishing, 2009 012073.

[74] H. Kim, F. Miyaji, T. Kokubo, T. Nakamura, Effect of heat treatment on apatite-forming ability of Ti metal induced by alkali treatment, J. Mater. Sci. Mater. Med. 8 (6) (1997) 341–347.

[75] X. Sun, Y. Li, Synthesis and characterization of ion-exchangeable titanate nanotubes, Chem. Eur. J. 9 (10) (2003) 2229–2238.

[76] M.H.A. Rehim, A.M. Youssef, H. Al-Said, G. Turky, M. Aboaly, Polyaniline and modified titanate nanowires layer-by-layer plastic electrode for flexible electronic device applications, RSC Adv. 6 (97) (2016) 94556–94563.

[77] Z.B. Bahşi, A. Büyükaksoy, S.M. Ölmezcan, F. Şimşek, M.H. Aslan, A.Y. Oral, A novel label-free optical biosensor using synthetic oligonucleotides from *E. coli* O157: H7: elementary sensitivity tests, Sensors 9 (6) (2009) 4890–4900.

[78] Y. Zhao, R.L. Frost, W.N. Martens, Synthesis and characterization of gallium oxide nanostructures via a soft-chemistry route, J. Phys. Chem. C 111 (44) (2007) 16290–16299.

[79] J. Shah, P. Ratnasamy, M.L. Carreon, Influence of the nanostructure of gallium oxide catalysts on conversion in the green synthesis of carbamates, Catalysts 7 (12) (2017) 372.

[80] S. Ramesh, C. Tan, M. Hamdi, I. Sopyan, W. Teng, The influence of Ca/P ratio on the properties of hydroxyapatite bioceramicsInternational Conference on Smart Materials and Nanotechnology in Engineering, International Society for Optics and Photonics 2007, p. 64233A.

[81] T. Kizuki, H. Takadama, T. Matsushita, T. Nakamura, T. Kokubo, Effect of Ca contamination on apatite formation in a Ti metal subjected to NaOH and heat treatments, J. Mater. Sci. Mater. Med. 24 (3) (2013) 635–644.

[82] X. Sun, Y. Li, Synthesis and characterization of ion-exchangeable titanate nanotubes, Chem. Eur. J. 9 (10) (2003) 2229–2238.

[83] H.M. Kim, F. Miyaji, T. Kokubo, T. Nakamura, Preparation of bioactive Ti and its alloys via simple chemical surface treatment, J. Biomed. Mater. Res. 32 (3) (1996) 409–417.

[84] J. Faure, A. Balamurugan, H. Benhayoune, P. Torres, G. Balossier, J. Ferreira, Morphological and chemical characterisation of biomimetic bone like apatite formation on alkali treated Ti6Al4V titanium alloy, Mater. Sci. Eng. C 29 (4) (2009) 1252–1257.

[85] P. Collery, B. Keppler, C. Madoulet, B. Desoize, Gallium in cancer treatment, Crit. Rev. Oncol. Hematol. 42 (3) (2002) 283–296.

[86] J. Chandler, H. Messer, G. Ellender, Cytotoxicity of gallium and indium ions compared with mercuric ion, J. Dent. Res. 73 (9) (1994) 1554–1559.

[87] M.A. Getzlaf, E.A. Lewallen, H.M. Kremers, D.L. Jones, C.A. Bonin, A. Dudakovic, R. Thaler, R.C. Cohen, D.G. Lewallen, A.J. Van Wijnen, Multi-disciplinary antimicrobial strategies for improving orthopaedic implants to prevent prosthetic joint infections in hip and knee, J. Orthop. Res. 34 (2) (2016) 177–186.

[88] H. Busscher, M. Rinastiti, W. Siswomihardjo, H. Van der Mei, Biofilm formation on dental restorative and implant materials, J. Dent. Res. 89 (7) (2010) 657–665.

[89] J. Raphel, M. Holodniy, S.B. Goodman, S.C. Heilshorn, Multifunctional coatings to simultaneously promote osseointegration and prevent infection of orthopaedic implants, Biomaterials 84 (2016) 301–314.

[90] D. Baldoni, A. Steinhuber, W. Zimmerli, A. Trampuz, In vitro activity of gallium maltolate against staphylococci in logarithmic, stationary, and biofilm growth phases: comparison of conventional and calorimetric susceptibility testing methods, Antimicrob. Agents Chemother. 54 (1) (2010) 157–163.

[91] A.R. Yazdi, M. Towler, The effect of the addition of gallium on the structure of zinc borate glass with controlled gallium ion release, Mater. Des. 92 (2016) 1018–1027.